Beam Diagnostics using Coherent Transition Radiation at the TESLA Test Facility Linac

K. Hanke
Deutsches Elektronen-Synchrotron DESY, D-22603 Hamburg

October 1997

Abstract

Coherent transition radiation from picosecond electron bunches was observed at the TESLA test facility linac using a photo-acoustic detector. The detector signal was used to optimize the machine setting to short bunches. The coherent spectrum was measured using a filter spectrometer as well as a Martin-Puplett interferometer. From the measured spectra, the bunch length could be obtained.

1 Introduction

Transition radiation is produced as charged particles pass through the interface of two materials with different dielectric properties. The radiation is emitted both in forward and backward direction. At the TESLA test facility linac, transition radiation is produced by moving thin aluminum targets into the beamline. By arranging the radiator at an angle of 45^o with respect to the electron beam direction, one can seperate the backward transition radiation from the electron beam and make use of it for beam diagnostics. While the visible part of the spectrum can be used for transverse imaging of the beam using optical techniques, the long-wavelength part of the spectrum can be used to obtain the bunch length. This technique, reported for sub-picosecond bunches ([1],[2],[3] and references therein), has been adapted for picosecond bunch length [4].

The total intensity emitted by a bunch of particles can be expressed as

$$I_{tot}(\lambda) = I_1(\lambda)[N + N(N-1)f(\lambda)] \tag{1}$$

where $I_1(\lambda)$ is the radiation intensity emitted by a single electron at wavelength λ and N is the number of particles in the bunch. The three-dimensional Fourier

transform of the normalized charge distribution $S(\mathbf{r})$

$$f(\lambda) = \left| \int_{-\infty}^{+\infty} dr S(\mathbf{r}) e^{\frac{2\pi i(\mathbf{n}\cdot\mathbf{r})}{\lambda}} \right|^2 \tag{2}$$

is called the bunch form factor. The co-ordinates are chosen such that $\mathbf{r}$ is the position vector of an electron and $\mathbf{n}$ is the unit vector directed from the observer to the particle. If the observation direction is along the z-axis and the particle bunch is symmetric in x and y, (2) simplifies to

$$f(\lambda) = \left| \int_{-\infty}^{+\infty} dz S(\mathbf{z}) e^{\frac{2\pi i z}{\lambda}} \right|^2 \tag{3}$$

and the form factor depends only on the longitudinal charge distribution $S(\mathbf{z})$. Due to the normalization

$$\int_{-\infty}^{+\infty} dr S(\mathbf{r}) = 1 \tag{4}$$

the form factor can have values between 0 and 1.

For wavelengths shorter than the bunch length, the form factor approaches 0. The emitted transition radiation is then incoherent and its intensity scales with the number of particles N in a bunch. It is characterized by the properties of the individual charges in a bunch and hence can be used for measuring these. In particular, the incoherent part of the spectrum can be used for transverse beam profile measurement, emittance measurement and energy measurement.

For wavelengths equal to the bunch length and longer, the form factor approaches unity. At sufficiently long wavelenghts, the whole bunch appears as one single particle ('macro-electron') with charge Ne. The emitted transition radiation is then coherent and its intensity scales with N^2. The coherent part of the spectrum carries information about the collective properties of the bunch. In particular, one can obtain from it information about the longitudinal charge distribution. In addition, the long wavelength radiation is much more intense than the incoherent part. A detailed derivation of the formalism can be found in [5],[6],[7].

2 Signal Detection

Since the bunch length at the TESLA test facility linac is supposed to be in the picosecond range, coherent transition radiation is expected at wavelengths of a few millimeters. For the detection of millimeter waves, a photo-acoustic power meter from Thomas Keating Ltd. was chosen [8]. It has a flat response from 0.1 mm up to 10 mm wavelength (3 THz - 30 GHz). The aperture of the detector is 30 $\times$ 60 mm^2. The power meter is a Golay-cell type detector consisting of a closed gas volume with a metal foil absorber inside [9]. A known fraction (49$\pm$2%) of the radiation directed onto the window is absorbed by the foil, the rest is partly transmitted and partly reflected. A hearing aid microphone powered by a 9 V battery is used to transform the change in pressure into a voltage. The time constant of the detector is in the order of 10 milliseconds. An incoming radiation pulse results in a steep increase of the detector output followed by a long decay.

3 Filter Spectrometer

A set of filters can serve, together with the broadband photo-acoustic detector, as a spectrometer [10]. A periodic pattern of holes drilled into a brass plate acts as a high-pass filter for millimeter waves [11], [12]. The holes behave like circular waveguides with a given cutoff wave number $\bar{\nu}_c$. The advantage of using an array of waveguides is that the radiation needs not to be directed through a single, small structure.

In a hollow cylindrical structure with conducting walls as sketched in Fig. 1, only TM and TE modes can propagate. Each of the various modes has its specific cutoff wave number $\bar{\nu}_c$. Above the cutoff wave number $\bar{\nu}_c$, radiation propagates almost lossless in the waveguide, whereas below $\bar{\nu}_c$ the field decays exponentially along z. The transmission T through such a waveguide is given by

$$T = \exp\{-2\gamma t\} \tag{5}$$

with

$$\gamma = \begin{cases} 0 & \text{for } \bar{\nu} > \bar{\nu}_c \\ 2\pi\sqrt{\bar{\nu}_c^2 - \bar{\nu}^2} & \text{for } \bar{\nu} < \bar{\nu}_c, \end{cases} \tag{6}$$

where t is the thickness of the plate. The exponential decay below cutoff provides a filter function with a very steep slope. The slope below cutoff becomes steeper as the guide length increases.

The value of $\bar{\nu}_c$ varies for different modes. The lowest cutoff is found for the TE_{11} mode. Its cutoff wave number is given by

$$\bar{\nu}_c = \frac{0.586}{d}, \tag{7}$$

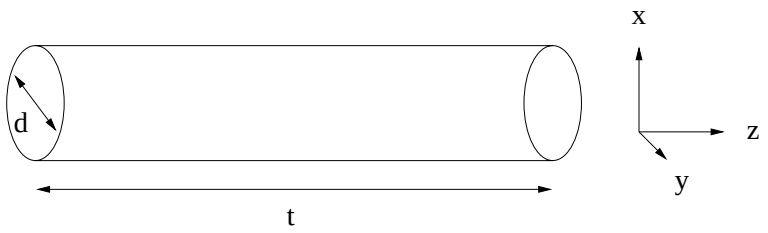

Figure 1: Circular cutoff waveguide with diameter d. The length is given by the thickness t of the plate.

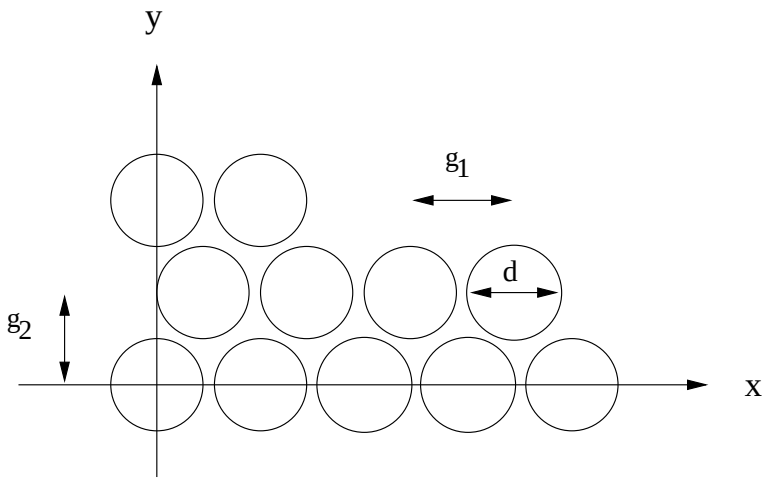

Figure 2: Geometry of a high-pass filter for millimeter waves.

where d is the diameter of the holes. Higher order modes have their cutoff at higher wave numbers than the fundamental mode.

The in- and outgoing radiation couples to the array of waveguides. The transmission approaches (5) the better the beams couple to the TE_{11} mode inside the waveguide. Unlike in the case of a single waveguide, where the outgoing radiation forms a very broad lobe, interference effects of an array of waveguides provide that the outgoing radiation is well collimated.

Figure 2 shows the geometry of a filter and Tab. 1 gives the dimensions for a set of filters with various cutoff wave numbers. The thickness of the brass plates is chosen at twice the diameter of the holes in oder to suppress long wavelengths sufficiently. The spacing of the holes provides closest possible packing of the waveguides. The transmission was specified to 85% for the cutoff wave number. Ten filters were manufactured by drilling patterns of holes into brass plates. The array of holes covers 50 mm $\times$ 50 mm, the total size of the filters is 60 mm $\times$ 60 mm. The transmission curves of a series of filters were measured

filter	d[mm]	$\bar{\nu}_c$ [cm$^-$1]	g_1[mm]	g_2[mm]	t [mm]
1	5.85	1.00	6.882	5.960	11.70
2	3.90	1.50	4.588	3.973	7.80
3	2.90	2.02	3.412	2.955	5.80
4	2.35	2.49	2.765	2.395	4.70
5	2.00	2.93	2.353	2.038	4.00
6	1.70	3.45	2.000	1.732	3.40
7	1.50	3.91	1.765	1.529	3.00
8	1.30	4.51	1.523	1.319	2.60
9	1.15	5.10	1.353	1.172	2.30
10	1.00	5.86	1.176	1.018	2.00

Table 1: Nominal parameters of high-pass filters.

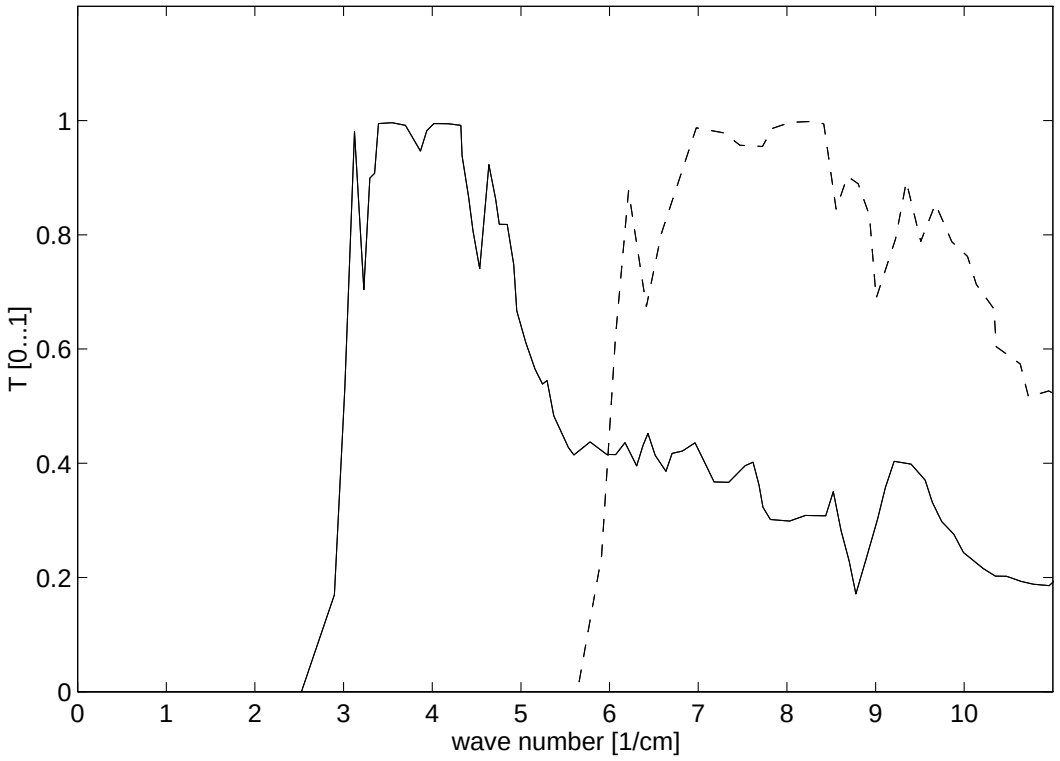

Figure 3: Measured transmission versus wave number for filters with cutoff wave numbers $\bar{\nu}_c = 2.93$ cm^{-1} and $\bar{\nu}_c = 5.86$ cm^{-1}.

over a whole frequency range [13], [14]. Figure 3 shows the measured curves for filters with nominal cutoff wave numbers $\bar{\nu}_c = 2.93$ cm^{-1} and $\bar{\nu}_c = 5.86$ cm^{-1}. As specified, the filters are non-transparent below cutoff. The transmission above cutoff is not constant but decays with the wave number and has several minima. This behaviour is caused by higher modes which have their cutoff at higher wave numbers. An important result is that the shape of the curves is equal for all filters and simply scales with $\bar{\nu}_c$. This allows to normalize the transmission curves with respect to the wave number and to calculate the general form of this curve. Using this general transmission curve, any filter can be characterized simply by scaling the curve to its specific cutoff wave number.

The highpass filters are mounted on a rotatable wheel. In addition to the 10 filters, there is an open window without filter and a completely closed section. The wheel is driven by a stepper motor such that the filters can be placed successively in front of the photo-acoustic detector which is mounted as close as possible to the filters. The filter spectrometer is placed directly at a transition radiation target such that the distance between the radiatior and the detector is as small as possible. The advantage of such a system is its simplicity. Since no quasi-optical setup is required, such a spectrometer can be used at low electron beam energy where the opening angle of the radiation is large. The filter spectrometer allows a direct measurement of the spectrum. Its resolution is of course limited by the number of filters available.

4 Martin-Puplett Interferometer

Interferometers can serve as spectrometers for electromagnetic waves. The principle of these measurements is called Fourier spectroscopy. By splitting up a radiation pulse into two equal parts and successively overlapping the two half pulses, the interferometer measures the autocorrelation function. From the measured autocorrelation, the spectrum can be obtained using the fact that the modulus squared of the Fourier transform of a pulse $f(t)$ equals the Fourier transform of its autocorrelation function $c_{ff}(t) = f(t) \odot f(t)$:

$$|F\{f(t)\}|^2 = F\{f(t) \odot f(t)\}. \tag{8}$$

Equation (8) is known as the Wiener-Khintchine relation [15]. It is illustrated for the special case of a flat pulse in Fig. 4.

For a flat charge distribution for example, the autocorrelation would be triangular shaped with a full width half maximum of the pulse length. This is strictly only true for an ideal spectrometer with a flat effieciency for all frequencies. Figure 5 shows in the upper left plot a flat charge distribution in the time domain and in the upper right plot its autocorrelation function. The autocorrelation function has been calculated without applying a filter, which corresponds to an ideal

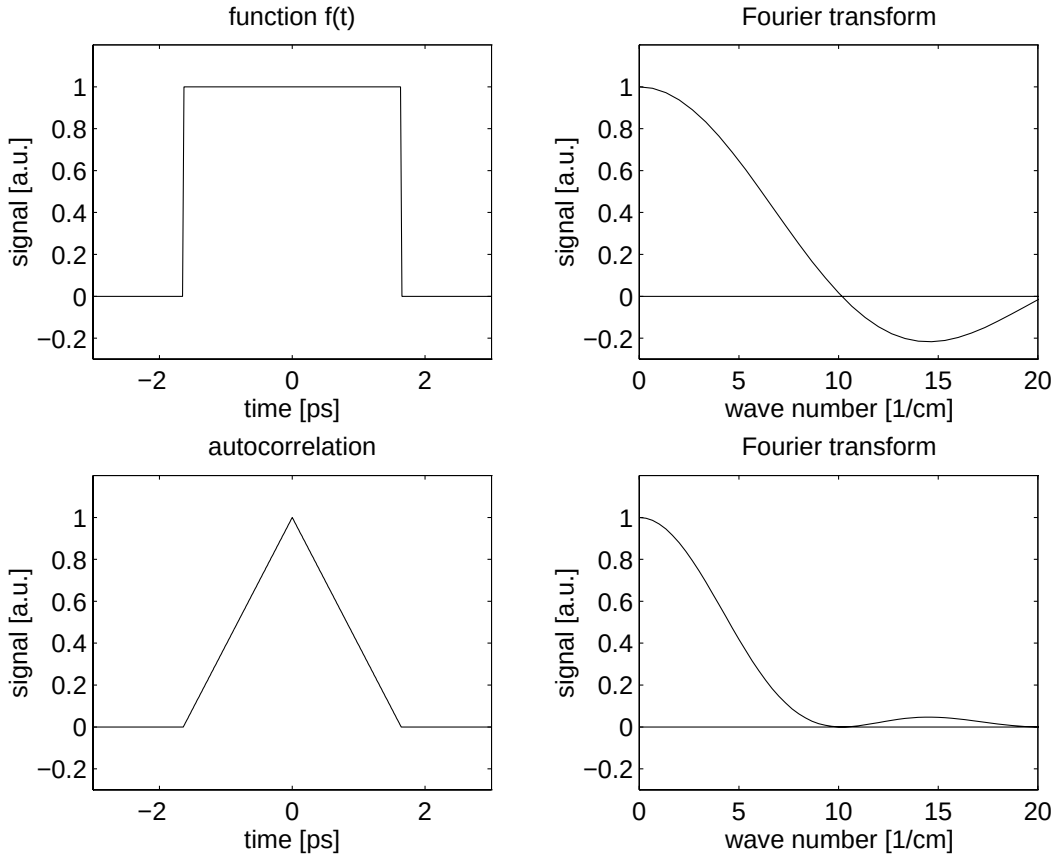

Figure 4: The modulus squared of the Fourier transform of a pulse $f(t)$ equals the Fourier transform of its autocorrelation function.

spectrometer. Any real instrument has a certain bandwidth. A low frequency cutoff due to the detector or optical components can be simulated by applying a high-pass filter to the pulse. The lower left plot shows the pulse in the time domain after applying a high-pass filter and the lower right plot the corresponding autocorrelation function.

The spectrum can be obtained by applying a numerical fast Fourier transform to the measured interferogram. Since the power spectrum does not contain the phase information, the bunch shape cannot directly be obtained from the spectrum. A possible way to obtain the bunch shape is to generate charge distributions in the time domain and then to transform them into the frequency domain. If the calculated spectrum is in good agreement with the one obtained from the interferogram, the bunch shape and length can be obtained.

For some charge distributions, the power spectrum is analytically known. These analytic functions can be used for a fit in the frequency domain and the corre-

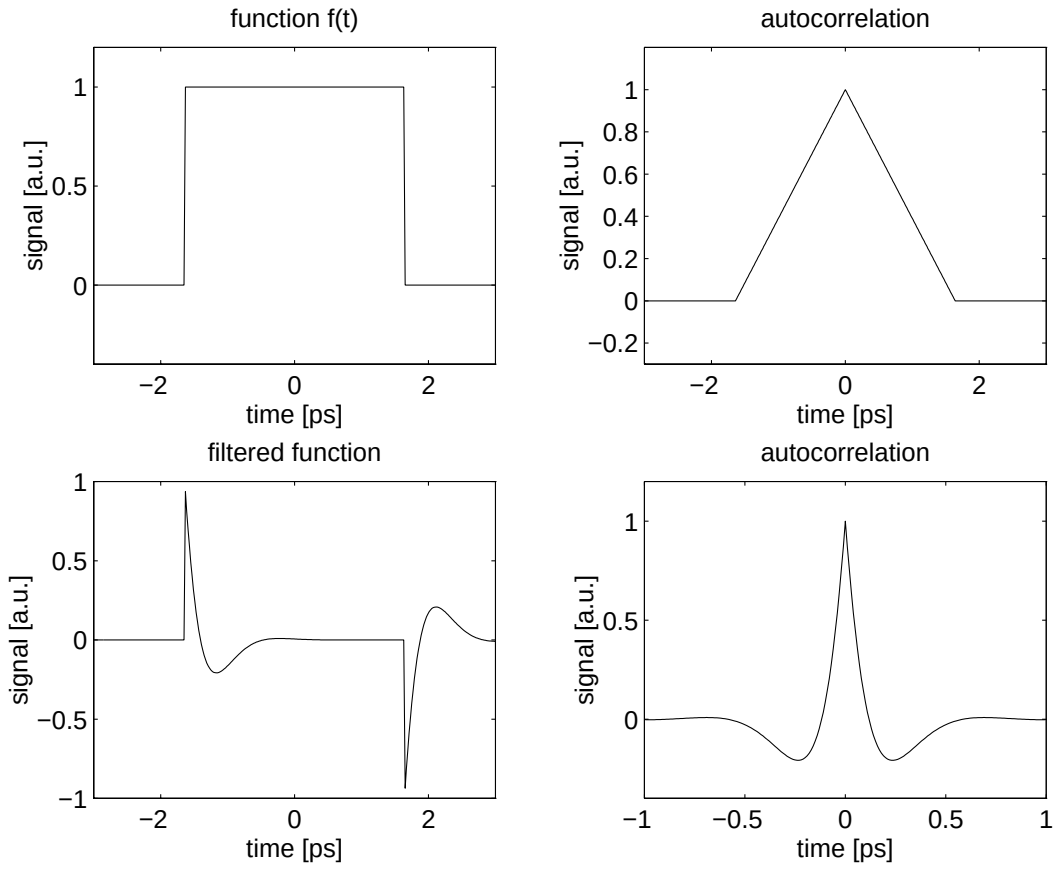

Figure 5: Pulse shape (upper left plot) and autocorrelation function (upper right plot). After applying a high-pass filter, the pulse shape changes (lower left plot). The corresponding autocorrelation function (lower right plot) has the same shape as the measured interferograms.

sponding charge distribution in the time domain be recalculated. For instance, the minima of a $sin(x)/x$ function in the frequency domain yield directly the length of a flat charge distribution in the time domain.

Since in general only the first maximum of the spectrum can clearly be seen, a Gaussian fit in the frequency domain is often a good choice. From the width of the distribution in terms of wavenumbers, the width in terms of frequency can be calculated according to $\omega = 2\pi c\bar{\nu}$. The sigma of the distribution in the time domain is then simply $\sigma_t = 1/\sigma_\omega$.

Various kinds of interferometers can be used for spectroscopy in the far infrared. For the frequency range of interest here, a Martin-Puplett interferometer was used [16], [17]. It is a system of wire grid polarizers and roof-mirror reflectors. Figure 6 shows the schematical setup of the interferometer. The incoming transi-

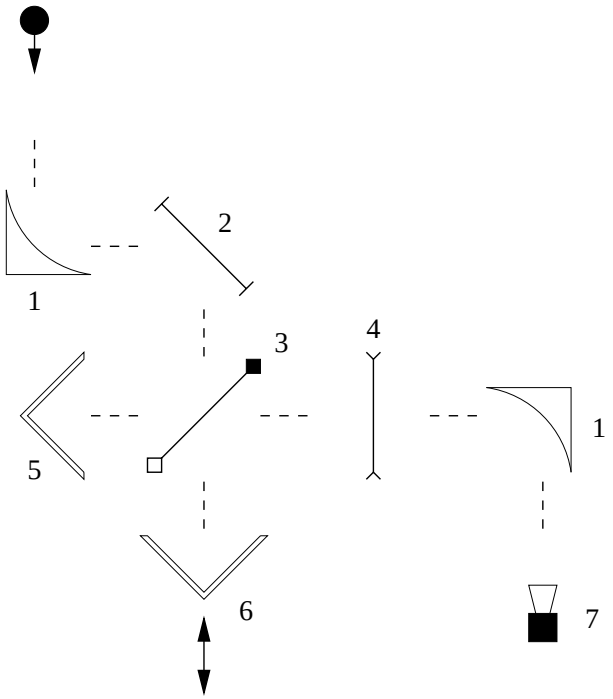

Figure 6: Schematical setup of the Martin-Puplett interferometer. 1: focusing mirrors; 2: polarizer; 3: beamsplitter; 4: analyzer; 5: fixed roof mirror; 6: movable roof mirror; 7: detector.

tion radiation falls on an off-axis paraboloid with a focal length of 200 mm. The interferometer is arranged such that the radiation source is in the focus of the mirror. The paraboloid is machined from aluminum and hand-polished.

The radiation is then reflected by a wire grid polarizer with the wires arranged horizontally with respect to the optical bench. The grids used for this setup are made from 20 μm tungsten wire at a spacing of 100 μm. The first grid reflects the polarization component with the electric vector oriented parallel with respect to the wires into the interferometer. The other polarization component is lost. This grid therefore acts as a polarizer.

The radiation is then passed to a second grid with the wires arranged at 45^o with respect to the polarization plane of the incoming beam. This grid acts as a beamsplitter. It reflects half of the incoming radiation and transmits the other half of it. Since it is arranged at 45^o with respect to the beam axis, one polarization component is passed to a fixed roof mirror, while the other polarization component is passed to a movable roof mirror. It should be noted, that the angle of the wires must be 45^o viewed along the input beam axis. That means that the beamsplitter grid must be mounted at an angle of 35^o with respect to the optical

bench.

The roof mirrors reflect the radiation and at the same time alter the polarization state, such that both beams are superimposed again. The movable roof mirror is mounted on a stepper motor driven translation stage. The maximum travel distance is 50 mm, that is 25 mm in both directions. The stepwidth can be chosen with a minimum of 2.5 μm. Upon changing the optical path difference, the polarization state of the recombined beam is rotated. They pass a third grid with its wires arranged vertically with respect to the optical bench. This grid acts as an analyzer which selects a polarization component.

The radiation is then focused onto the detector by a second off-axis paraboloid. The power measured by the detector as a function of the path difference yields the autocorrelation of the radiation pulses.

The Martin-Puplett interferometer was designed and built with a flat efficiency over the whole millimeter wavelength range. Another advantage of the Martin-Puplett interferometer is, that after the first polarizer all the radiation power is directed to the detector and nothing is directed back to the source as in the case of the Michelson interferometer. All components have an aperture of 80 mm to avoid diffraction limitations at long wavelengths. The whole setup is installed on a 500 $\times$ 500 mm optical bench.

The interferometer was operated with the photo-acoustic detector. The detector output is amplified in the accelerator tunnel and the amplified signal transmitted to the control room where it is read out by an oscilloscope or analog-digital converter.

5 Results

5.1 Observation of Coherent Transition Radiation

Coherent transition radiation was observed using the photo-acoustic detector. The beam energy was about 80 MeV and the single bunch charge 10^8 particles. The beam consisted of macropulses with 30 μs length and the bunch spacing was 4.6 ns. The repetition rate of the macropulses was 2 Hz. Figure 7 shows the output voltage of the detector viewed on an oscilloscope.

The detector output is very sensitive to beam current and bunch length. In order to verify the non-linear behaviour of the radiation power, the beam current was varied and the detector output measured. Figure 8 shows the detector output as a funcion of the beam current. The non-linear increase of the radiation power can clearly be observed. This test of the theoretically predicted bahaviour can be used to verify that the detector signal is really due to coherent radiation.

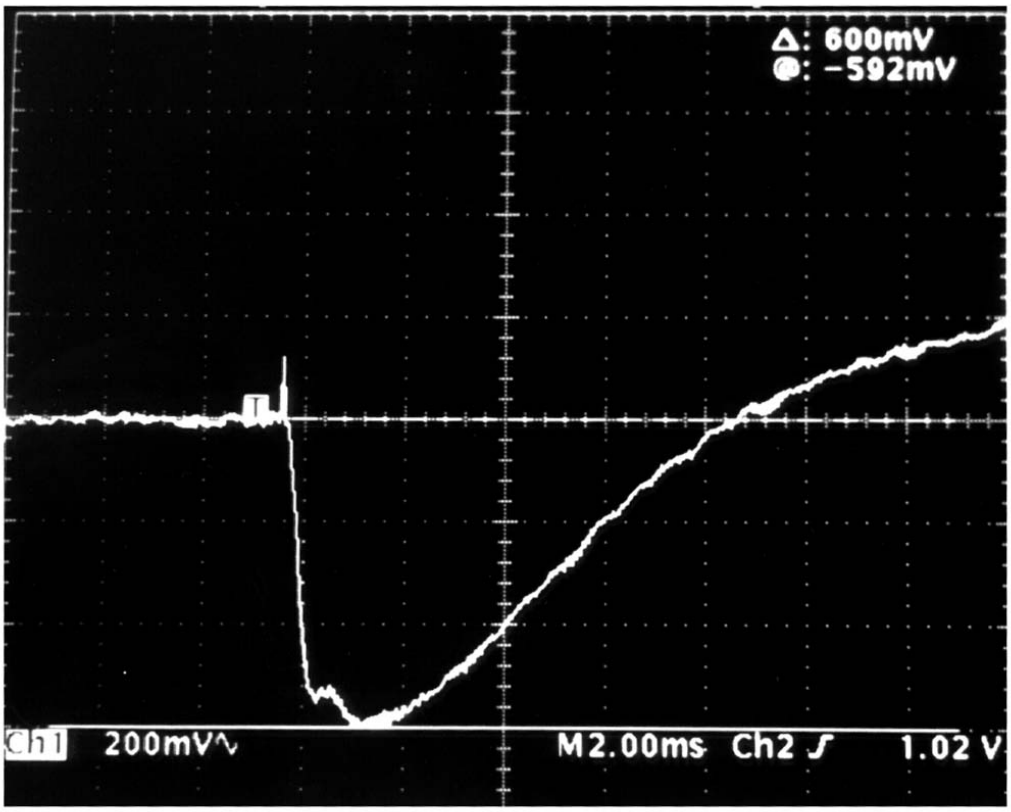

Figure 7: Output voltage of the photo-acoustic detector viewed on an oscilloscope. The polarity of the signal is negative. The time constant of the detector is in the order of 10 ms.

5.2 Optimization of Machine Setting

Since the detector output is extremely sensitive to the bunch length, the detector output can be used to optimize the machine to short bunches. The voltage of the subharmonic prebuncher was changed in order to minimize the bunch length. Figure 9 shows the detector output as a function of the prebuncher voltage. The machine can be optimized to a short bunch length by maximizing the detector signal. The best setting is found at 515 scale divisions. While changing the prebuncher voltage had a significant effect on the detector output, it was less sensitive to a change of the phase.

5.3 Estimate of Bunch Length from Energy Spread

For the optimized machine setting, the bunch length was estimated from the energy spread. The trajectory of a charged particle through an accelerator can

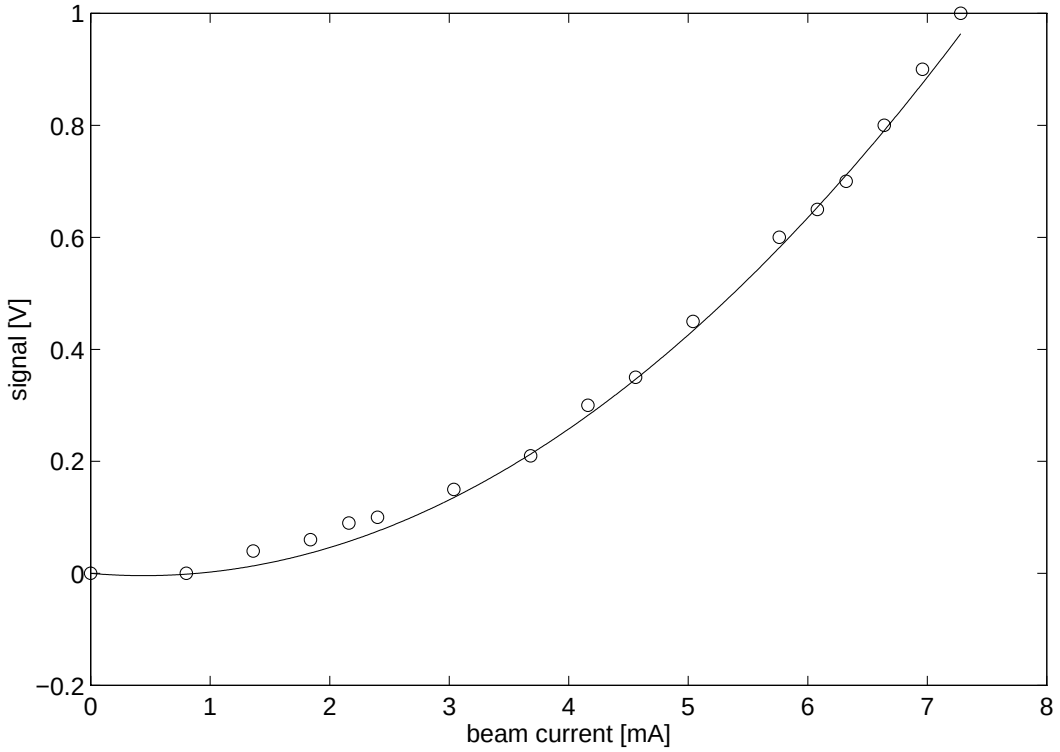

Figure 8: Output of photo-acoustic detector versus beam current. The expected non-linear dependence can clearly be seen.

be described using a matrix formalism [18]. At any position, the particle is represented by a vector $\mathbf{X}$. The transport of a particle through an accelerator section is represented by multiplication with a transport matrix $\mathbf{R}$ such that

$$\boldsymbol{X}(1) = \boldsymbol{R}\boldsymbol{X}(0), \tag{9}$$

where $\mathbf{X}(0)$ is the initial coordinate vector and $\mathbf{X}(1)$ is the final coordinate vector of the particle under consideration. For the beam transport through the acceleration section of a linear accelerator, one obtains an expression for the energy spread δ:

$$\delta(1) = R_{56}l + R_{66}\delta(0), \tag{10}$$

where the elements R_{56} and R_{66} of the transport matrix are given by

$$\begin{aligned} R_{56} &= \left(\frac{\Delta E \sin\phi}{E_0 + \Delta E\cos\phi}\right)\frac{2\pi}{\lambda}, \\ R_{66} &= \frac{E_0}{E_0 + \Delta E\cos\phi}. \end{aligned} \tag{11}$$

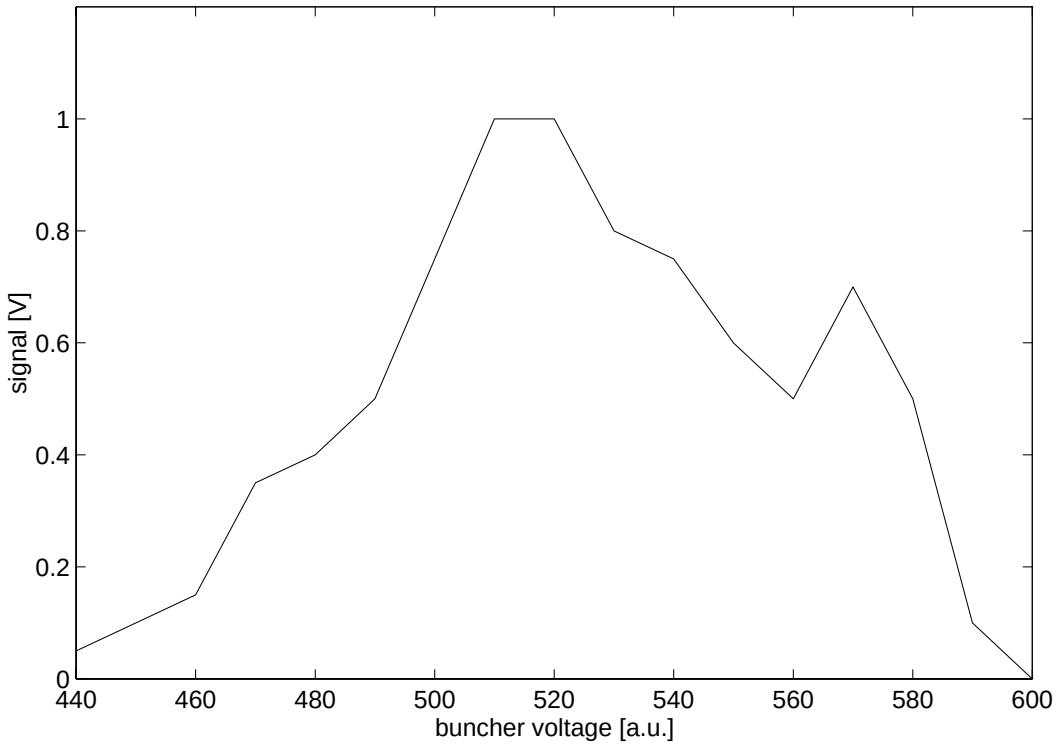

Figure 9: Total output of photo-acoustic detector versus buncher setting. At the setting with the shortest possible bunch length, the detector signal has its maximum.

Here, λ is the wavelength of the accelerating field, E_0 is the beam energy in front of the accelerating section, ΔE is the energy gain in the acceleration module and ϕ is the phase lag of the reference particle behind the crest of the accelerating wave.

The energy spread $\delta(0)$ behind the injector at 10 MeV and $\delta(1)$ behind the acceleration module was measured. From this, an estimate of the bunch length of $\sigma \approx 1$ mm ($\hat{=}$3.3 ps) was obtained.

5.4 Measurements with Filter Spectrometer

For the same machine setting, the spectrum of the coherent transition radiation was measured with the filter spectrometer. The filters are moved successively between the photo-acoustic detector and the vacuum window of the transition radiation monitor. The detector output voltage is measured for each filter. Figure 10 shows the measured spectrum. Since the resolution of such a measurement is limited, an assumption on the bunch shape must be made. A Gaussian charge

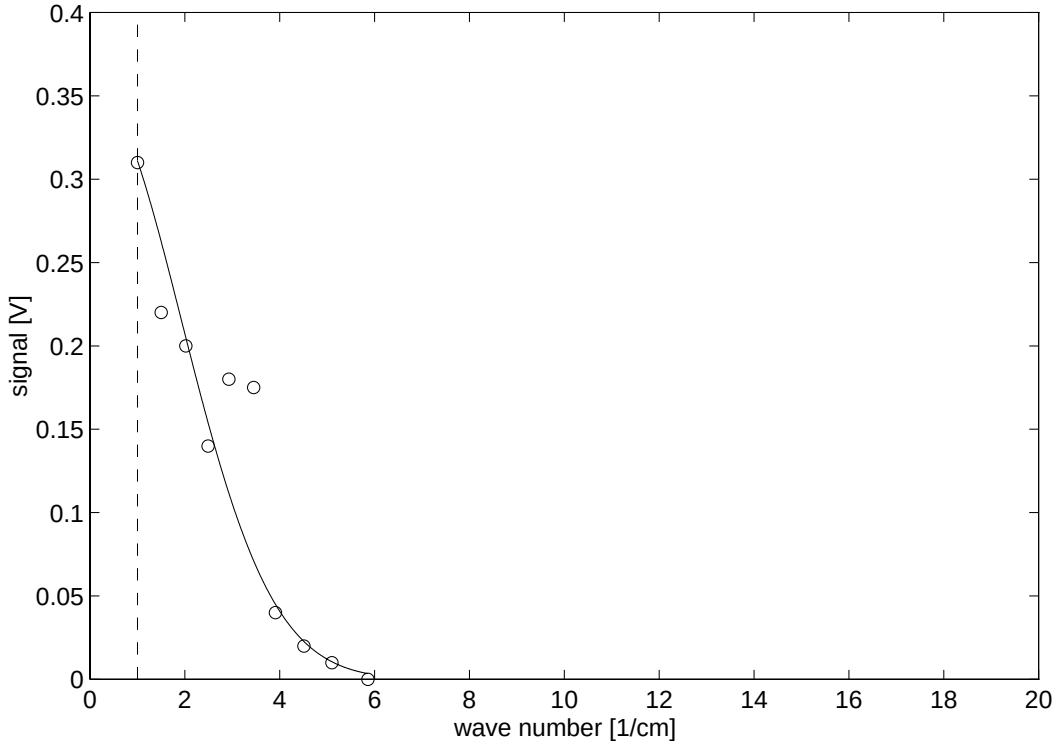

Figure 10: Spectrum of coherent tranistion radiation measured with the filter spectrometer. A Gaussian fit to the spectrum yields a bunch length of $\sigma = 2.76$ ps in the time domain.

distribution which results in a Gaussian shape of the spectrum was chosen. From a Gaussian fit applied in the frequency domain, a Gaussian charge distribution in the time domain with $\sigma = 2.76$ ps is obtained. This is in good agreement with the estimate from the energy spread.

5.5 Measurements with Interferometer

The autocorrelation of the bunch shape was measured with the Martin-Puplett interferometer. The stepwidth was chosen to 25 μm and the total travel distance of the movable mirror to 5 mm. The mechanical path length difference can directly be transformed in an optical path length difference in terms of picoseconds. Figure 11 shows the interferometer scan. Each point was averaged over 30 single measurements. The central peak as well as two side minima are clearly seen. In order to suppress the high frequent noise, which is superimposed to the autocorrelation, a polynomal fit is applied. The fit is shown as a dashed line in Fig. 11. From the measured autocorrelation function, the spectrum can be calculated.

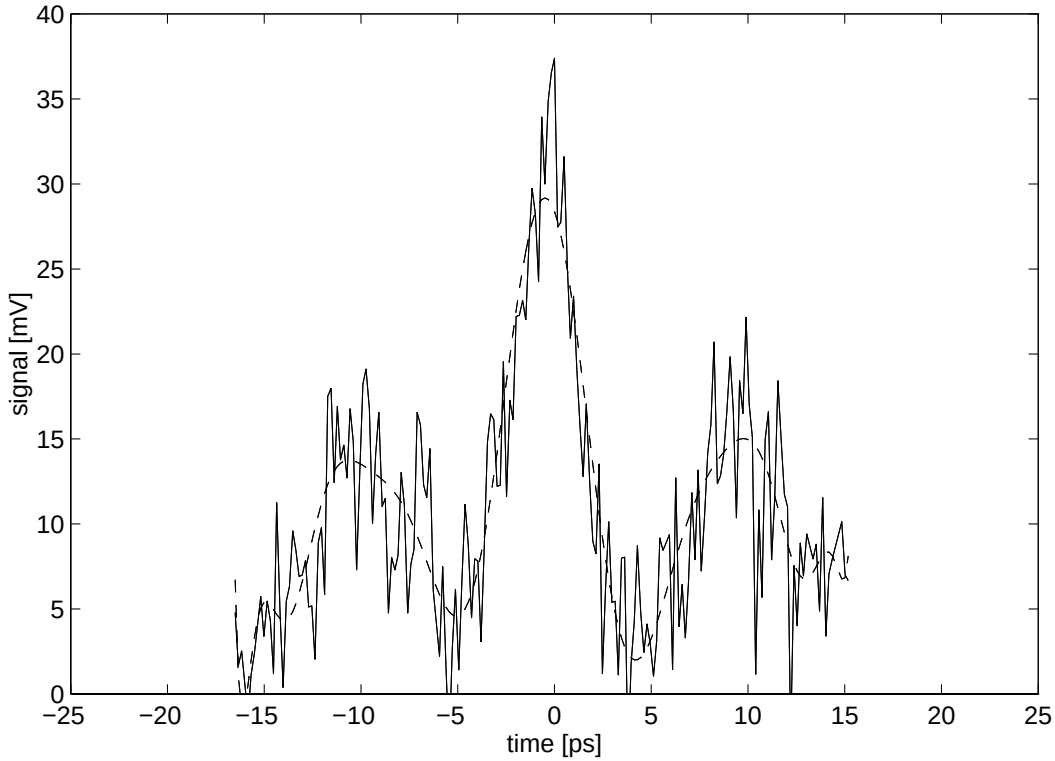

Figure 11: Autocorrelation of TTFL bunches. The detector output is plotted versus the optical path length difference of the interferometer arms. The solid line shows the measured data, the dashed line is a ploynomial fit which suppresses high frequent noise.

Figure 12 shows the power spectrum obtained by applying a Fourier transform to the fitted curve. The low frequency cutoff is found at about 3 wavenumbers. Since the cutoff due to the limited bandwith of the detector is expected at 1 cm^{-1}, apparently the optical setup itself causes a further limitation due to diffraction or highpass action of components. Above cutoff, the decay of the first maximum can clearly be seen. A Gaussian fit performed to the first maximum yields a bunch length in the time domain of $\sigma_t = 2$ ps. It should be noted, that this measurement was done at a different machine setting than the measurement with the filter spectrometer.

6 Conclusion and Outlook

Coherent transition radiation was observed at the TESLA test facility linac using a photo-acoustic detector. The theoretically predicted non-linear increase of the coherent radiation power with increasing bunch charge could be observed. Since

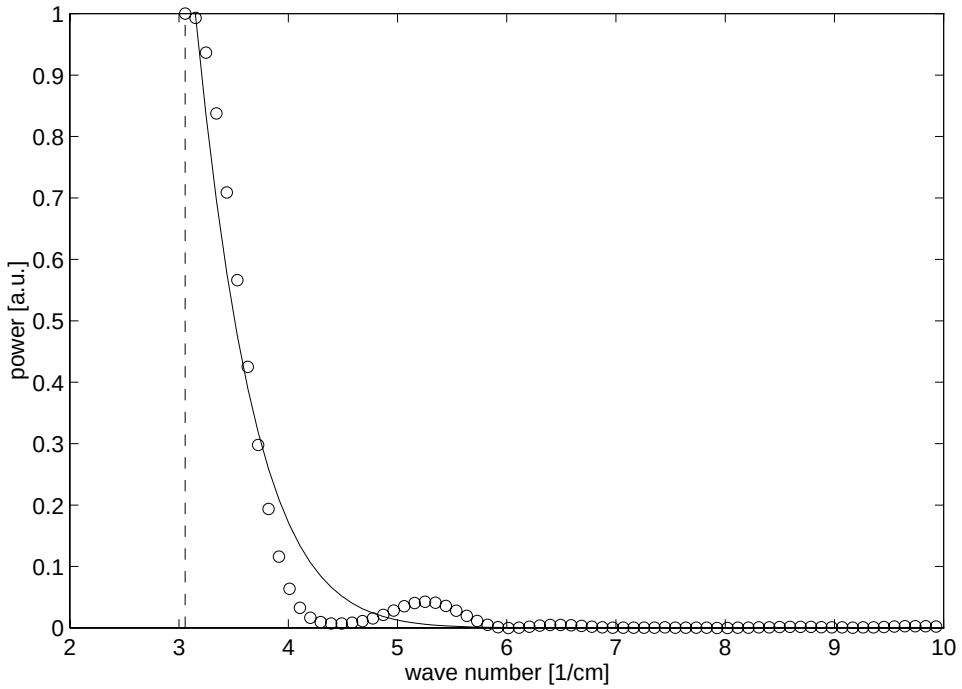

Figure 12: Spectrum calculated from the measured autocorrelation. The low frequency cutoff is found at $\bar{\nu} \approx 3$ cm^{-1} (vertical dashed line). The circles represent the data obtained from the Fourier transform, the solid line is a Gaussian fit. Assuming a Gaussian charge distribution, the fit yields $\sigma = 2$ ps.

the integrated detector output is very sensitive to the bunch length, it could be used to optimize the machine setting to short bunches. In particular the prebuncher voltage had significant influence on the bunch length.

Two types of spectrometers for millimeter waves were developed and constructed for bunch length measurements at the TESLA test facility linac. A filter spectrometer was used for a direct measurement of the coherent spectrum. The bunch length could be determined to $\sigma = 2.76$ ps assuming a Gaussian charge distribution.

A Martin-Puplett interferometer was used for a more precise measurement of the spectrum. It has an intrinsic flat efficiency over a wide wavelength range. From the measured autocorrelation of the bunches, again the spectrum can be obtained. From the spectrum, the bunch length could be determined to $\sigma = 2$ ps (Gaussian distribution).

A new method to measure the coherent spectrum was for the first time used for bunch length measurements at the TESLA test facility linac. The spectrometer is based on a Josephson junction. The characteristic line of the junction is

distorted under the influence of millimeter wavelength radiation. This effect can be used to determine the radiation spectrum applying a Hilbert transform [19]. First measurements indicated that the spectrometer is extremely sensitive and fast. Based on this technology, an ultrafast and non-destructive bunch length monitor will be developed [20].

Acknowledgements

I would like to thank all colleagues from DESY and the collaborating institutes who contributed to the setup and commissioning of the TESLA test facility linac.

In particular I would like to thank Dr. Michele Castellano and Dr. Luciano Catani as well as all the colleagues from INFN Frascati who provided the transition radiation setups for the TESLA test facility which served as a radiation source for the bunch length monitors.

For technical support I would like to thank Kurt Escherich, Rainer Fischer, Otto Peters, Tomasz Plawski and Bernd Sarau.

The workshop of the physics institute IIIA, RWTH Aachen, manufactured several parts of the experimental setup, in particular the high-pass filters.

References

[1] H. Lihn, D. Bocek, P. Kung, C, Settakorn, H. Wiedemann, *Measurement of Subpicosecond Electron Pulses*, Physical Review E, **Vol. 53**, No. 6 (1996).

[2] Y. Shibata, T. Takahashi, T. Kanai, K. Ishi, M. Ikezawa, J. Ohkuma, S. Okuda, T. Okada, *Diagnostics of an Electron Beam of a Linear Accelerator using Coherent Transition Radiation*, Physical Review E, **Vol. 50**, No. 2 (1994).

[3] R. Lai, U. Happek, A. J. Sievers, *Measurement of the Longitudinal Asymmetry of a Charged Particle Bunch from the Coherent Synchrotron or Transition Radiation Spectrum*, Physical Review E, **Vol. 50**, No. 6 (1994).

[4] K. Hanke, dissertation, Universität Hamburg, in preparation.

[5] C. J. Hirschmugl, M. Sagurton, G. P. Williams, *Multiparticle Coherence Calculations for Synchrotron-Radiation Emission*, Physical Review A, **Vol. 44**, No. 2 (1991).

[6] J. S. Nodvick, D. S. Saxon, *Suppression of Coherent Radiation by Electrons in a Synchrotron*, Physical Review, **Vol. 96**, No. 1 (1954).

[7] E. B. Blum, U. Happek, A. J. Sievers, *Observation of Coherent Synchrotron Radiation at the Cornell Linac*, Nucl. Instr. Meth. A307 (1991).

[8] Installation and Operating Instructions for the TK TeraHertz Absolute Power/Energy Meter Head , Thomas Keating Ltd.

[9] H. A. Zahl, M. J. E. Golay, *Pneumatic Heat Detector* , The Review of Scientific Instruments, **Vol. 17**, No. 11 (1946).

[10] K. Hanke, V. Schlott, K. Aulenbacher, H. H. Braun, F. Chautard, *Beam Diagnostics using Coherent Transition Radiation at the CLIC Test Facility*, CERN CLIC Note 298 (1996).

[11] F. Keilmann, *Infrared High-Pass Filter with High Contrast* , Intern. Journal of Infrared and Millimeter Waves, **Vol. 2**, No. 2, p. 259 (1981).

[12] A. Roberts, M.L. von Bibra, H.-P. Gemünd, E. Kreysa, *Thick Grids with Circular Apertures: a Comparison of Theoretical and Experimental Performance*, Intern. Journal of Infrared and Millimeter Waves, **Vol. 15**, No. 3, p. 505 (1994).

[13] H.-P. Gemünd, private communication.

[14] G. Busse, report on measurements carried out at Institut für Hochfrequenztechnik, Technische Hochschule Braunschweig, not published.

[15] E. Hecht, *Optics*, Addison-Wesley (1974/1987).

[16] J. Lesurf, *Millimetre-Wave Optics, Devices & Systems*, Adam Hilger, Bristol (1990).

[17] D. H. Martin, E. Puplett, *Polarised Interferometric Spectroscopy for the Millimetre and Submillimetre Spectrum*, Infrared Physics, **Vol. 10**, p. 105 (1969).

[18] K. L. Brown, D. C. Carey, C. Iselin, F. Rothacker, *Transport - A Computer Program for Designing Charged Particle Beam Transport Systems*, CERN 80-04.

[19] Y. Y. Divin, H. Schulz, U. Poppe, N. Klein, K. Urban, V.V. Pawlowskii, *Millimeter-wave Hilbert-transform spectroscopy with high-T_c Josephson junctions* , Appl. Phys. Lett. 68 (11) (1996).

[20] Y. Y. Divin, M. Geitz, K. Hanke, U. Poppe, to be published as TESLA report.